3-1-2009

Modeling and Simulation of Coating Growth on Nanofibers

J. Wilder

C. B. Clemons

K. L. Kreider

G. W. Young

Edward A. Evans
University of Akron Main Campus, evanse@uakron.edu

See next page for additional authors

Modeling and simulation of coating growth on nanofibers

J. Wilder,[1] C. B. Clemons,[1] K. L. Kreider,[1] G. W. Young,[1,a)] E. Evans,[2] and G. Zhang[2]
[1]*Department of Theoretical and Applied Mathematics, University of Akron, Akron, Ohio 44325-4002, USA*
[2]*Department of Chemical Engineering, University of Akron, Akron, Ohio 44325-3906, USA*

(Received 17 September 2008; accepted 31 December 2008; published online 13 March 2009)

This work presents modeling and simulation results of a procedure to coat nanofibers and core-clad nanostructures with thin film materials using plasma enhanced physical vapor deposition. In the experimental effort that motivates the modeling, electrospun polymer nanofibers are coated with metallic materials under different operating conditions to observe changes in the coating morphology. The modeling effort focuses on linking simple models at the reactor, nanofiber, and atomic levels to form a comprehensive model. Numerical simulations that link the concentration field with the evolution of the coating free surface predict that as the Damköhler number is increased the coating morphology changes from a wavy to a nodular to a dendritic needle-type form as observed experimentally. © *2009 American Institute of Physics*. [DOI: 10.1063/1.3080128]

I. INTRODUCTION

Electrospun-nanofiber-based structures are being developed for many different applications including energy conversion, filtration, composite reinforcement, and tissue engineering scaffolds.[1–3] The nanofibers are being incorporated into the structures to take advantage of their large surface area to mass ratio. For example, in energy conversion, emitting structures can be heated uniformly and maintain mechanical stability when made of small fiber scaffolds that support the emitting material. In filtration, the overall capture efficiency increases when nanofibers are incorporated into the filter media and evenly dispersed throughout the media. The properties of these structures will rely, at least in part, on the interface between the nanofibers and the surrounding material or media. In ceramic matrix composites, for example, one would like to have a weak interface between the fiber and the matrix. To achieve the desired properties, the surface of the nanofibers must be controlled. The nanofiber surface may be controlled by the synthesis approach or through post-processing. In the latter situation the surfaces can be modified after synthesis using liquid[4] or vapor phase techniques.[2,5–7]

This paper is a continuation of Refs. 8–11. Those works presented a coordinated experimental and modeling program for the synthesis of core/clad and hollow nanowire structures. Physical vapor deposition techniques were used to apply coatings to electrospun polymer nanofibers. These fibers have been coated with films of copper, aluminum, titanium, zirconium, and aluminum nitride by using a plasma enhanced physical vapor deposition (PEPVD) sputtering process.[11,12] The fiber samples were supported 8 cm above a sputtering target and the reactor operating conditions varied pressures between 4 and 40 mTorr and power between 30 and 150 W.

Figures 1(a)–1(c) show poly(*m*-phenylene isophthalamide) (MPD-I) nanofibers coated with aluminum nitride. The approximate thickness of the coating was controlled by the sputtering process. The coating morphologies (labeled wavy, nodular or needle type) shown in Figs. 1(a)–1(c) were observed as the deposition rate was increased. The deposition rate was increased by increasing the ratio of argon to nitrogen in the PEPVD reactor; the larger ratio of argon creates a more intense plasma leading to increases in sputtering and the rate of deposition.

The previous works[8–11] derived and solved the model both analytically and numerically under restrictive assumptions. In particular, Ref. 9 assumed a single-valued coating morphology, a nearly circular coating, and a concentration field that was only radially dependent and that was independent of the location of the coating-free surface. Reference 10 removed these assumptions but considered a parameter set that was restricted to small values of the Damköhler number. Reference 11 placed no restrictions on the Damköhler number but kept the single-valued assumption. Under these assumptions the analytical calculations and numerical simulations in the previous works predicted the development of the wavy coating morphology, as shown in Fig. 1(a) but did not predict any of the other morphologies. Based upon benchmarking studies of the model against experimental data as processing parameters are varied, it appears that the model we have developed predicts trends for the coating evolution on nanoscale structures that agree with experimental observation. Specifically, operating conditions that lead to high quantities of coating material (concentration C^* in the discussion to follow) result in thicker and rougher coatings. The coating thickness also increases with increasing initial fiber diameter. The coating roughness increases with increasing initial fiber diameter, pressure, and power, and decreasing nanofiber mat porosity. However, increases in power lead to an increase in etching at the coating surface. This could result in a decrease in coating thickness.

The present work does not impose the above restrictive assumptions and considers numerical simulations of the concentration field that couple with level set simulations of the evolution equation for the coating free surface. Hence, this

a)Electronic mail:gwyoung@uakron.edu.

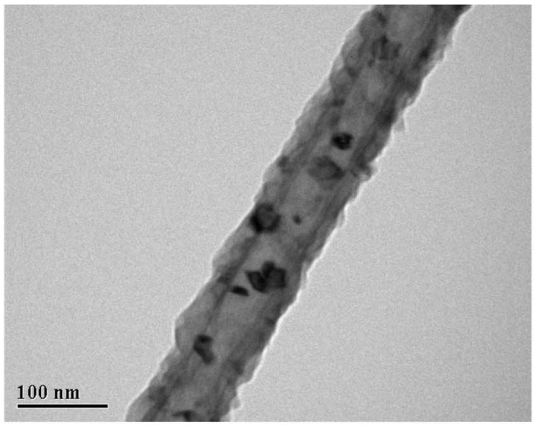

(a)

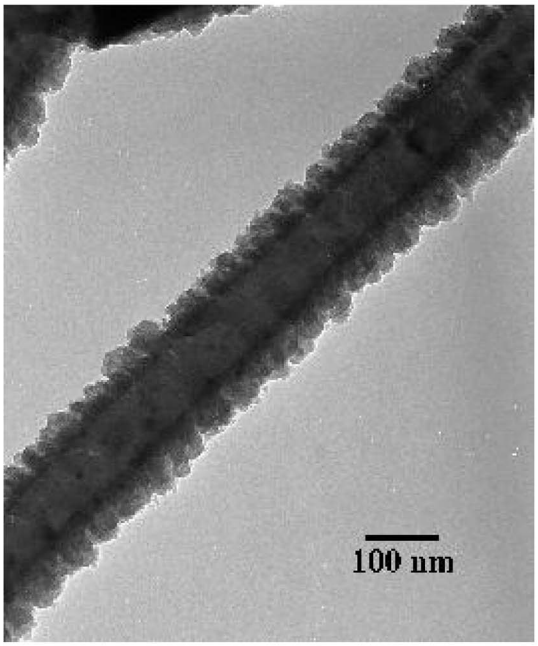

(b)

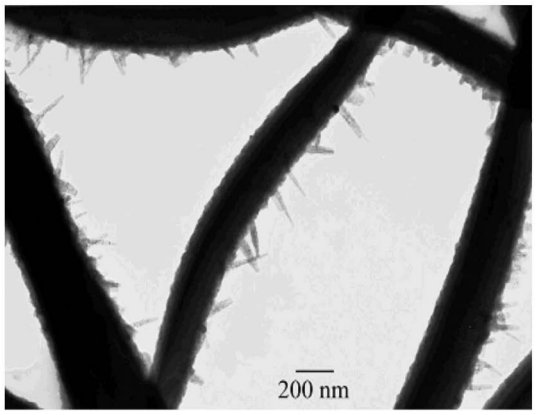

(c)

FIG. 1. TEM images of aluminum nitride coated nanofibers. (a) Wavy coating morphology. (b) Nodular coating morphology. (c) Needle-type coating morphology.

work not only verifies the simplifications made in previous analyses, but also considers operating regimes not accessible under the simplifying assumptions. The model simulations predict that as the Damköhler number (the ratio of the rate of deposition on the fiber to the rate of neutral species transport by diffusion) is increased the coating morphology changes from a wavy to a nodular to a needle-type form as observed experimentally and shown in Figs. 1(a)–1(c). Hence, this paper suggests that variation in the rate of deposition, as measured by the Damköhler number, provides a possible explanation for the occurrence of different coating morphologies as observed experimentally. Unfortunately, we do not know the value of the Damköhler number in the experiments that generated Fig. 1.

II. SINGLE FIBER COATING MODEL

To aid the understanding of the deposition process, a comprehensive model for the coating of nanofibers within a traditional PEPVD system was described in Refs. 8–11. In this model the transport of neutral species is separated into two components: (1) a one-dimensional reactor-scale model[8] and (2) a two-dimensional local nanofiber-scale model.[9–11] These models are linked as follows: the reactor-scale model provides the far-field (half the distance away from an adjacent fiber) input of the neutral species concentration, C^*. At the local nanofiber scale, a polar coordinate geometry is considered in Refs. 9 and 11, while an axisymmetric geometry is discussed in Ref. 10. Level set and evolution equation approaches are used to simulate the coating shape. Four basic components of the coating mechanism are included in these approaches. These are attachment kinetics, curvature effects, etching due to ion bombardment, and surface diffusion on the coating front. These equations were solved analytically and numerically under a variety of limiting assumptions as discussed above. This manuscript eliminates all of these assumptions and presents a numerical simulation of the full problem for both polar and axisymmetric geometries.

A. Model formulation

In Ref. 8 the dimensional concentration C^* of the neutral species at the reactor scale was found to be the constant,

$$C^* = \frac{k_{\text{ions}}}{k}, \tag{1}$$

where k is a reaction coefficient for sputtered material readsorbing to the target surface and k_{ions} is the desorption rate coefficient for sputtering due to ion bombardment of the target surface. These rate coefficients depend on the collisions between ions and neutral atoms, the ion flux to the surface, and the ion kinetic energy. These quantities are functions of the reactor pressure and power supplied to the target, which determine the ion number density, $\hat{n}_p$, in the plasma. The number density increases with the power and pressure and is most sensitive to changes in the power[13] under the reactor operating conditions used. The applied power and the pressure are both assumed controllable and therefore specified by the operator. Therefore, all constants that appear within this model are either material properties or can be experimentally controlled, at least in principle. Values for k and k_{ions} are listed in Figs. 7–9 of Ref. 8. These values are listed in Table I and used in the calculations below.

TABLE I. Parameter values.

Parameter	Value
C^*	1.5×10^{-36} mole/nm^3
$\hat{\Gamma}$	0.0505 nm
$\psi_s D_s$	6.5×10^{-3} nm^3/s
$\hat{D}$	6×10^{14} nm^2/s
$\hat{S}_F$	300 nm
k	3.0×10^{11} nm/s
k_{ions}	4.5×10^{-25} mole/nm^2 s
k_F	1.0×10^{13} mole/nm^2 s
$k_{F_{\text{ions}}}$	5.58×10^{-26} mole/nm^2 s

Hence, the concentration C^* is determined in the reactor as a function of the reactor operating conditions. This concentration field serves as the far-field input for the local transport model. We assume that the nanofiber mesh is sparse and that the concentration C^* away from a nanofiber is unaffected by any loss of depositing species due to deposition. This approximation is valid for fibers spaced several diameters apart as discussed in Ref. 11. Note also that the units of concentration are mole/volume, the units of k are length/time, and the units of k_{ions} are mole/(area$\times$time).

For the local nanofiber-scale transport model around a single nanofiber, we consider a polar geometry for discussion purposes although we present results for an axisymmetric geometry as well. The goal is to determine the location, $\hat{r}=\hat{F}(\theta,\hat{t})$, of the front of the deposited coating. Assume the source of the deposition material is given by C^*, and is located at $\hat{r}=\hat{S}_F$, where $\hat{S}_F$ is half the average spacing between fibers in the mat. Since C^* is a result of the sputtering process and depends on the reactor operating conditions, we have linked the *local and global* models through the condition at $\hat{r}=\hat{S}_F$.

Within the local region surrounding a fiber $[\hat{F}(\theta,\hat{t})\leq\hat{r}\leq\hat{S}_F]$, assume that the concentration $\hat{c}$ of deposition precursors (neutral gas molecules) is large compared to the ion concentration, and that the mode of transport of the deposition material is primarily governed by diffusion,

$$\hat{c}_{\hat{t}}=\hat{D}\left[\hat{c}_{\hat{r}\hat{r}}+\frac{1}{\hat{r}}\hat{c}_{\hat{r}}+\frac{1}{\hat{r}^2}\hat{c}_{\theta\theta}\right], \tag{2}$$

where $\hat{D}$ is the diffusivity. In this equation and in the following equations subscripts denote partial differentiation with respect to the subscripted variable.

At the coating front $[\hat{r}=\hat{F}(\theta,\hat{t})]$, the diffusive flux of neutral species equals the net rate of deposition due to (i) deposition (or reaction) from the bulk phase and (ii) desorption due to ion bombardment of the coating surface. These two processes correspond to the respective terms on the right hand side of the boundary condition,

$$\hat{D}\,\nabla\hat{c}\cdot\hat{n}=k_F\hat{c}[1-\hat{\Gamma}\hat{\kappa}]-k_{F_{\text{ions}}}. \tag{3}$$

Here k_F is a reaction coefficient, $\hat{\Gamma}$ is the capillary length scale, $\hat{\kappa}$ is the curvature of the front, and $k_{F_{\text{ions}}}$ is the desorption rate coefficient due to ion bombardment of the coating surface. Both k_F and $k_{F_{\text{ions}}}$ vary with the collisions between ions and neutral atoms, the power and pressure, and are obtained from Fig. 10 of Ref. 9. Further, as shown in Ref. 9, these quantities also vary with the angle of incidence of the bombarding ions. Thus, it is possible that in an array of fibers, individual fibers may experience different values of k_F and $k_{F_{\text{ions}}}$. This observation will be elaborated upon in the results section. Typical values for k_F and $k_{F_{\text{ions}}}$ are listed in Table I.

The normal velocity of the coating front, $\hat{v}_n$, is needed to simulate the film growth at this length scale, using the level set method. The normal front velocity is taken to be

$$\hat{v}_n=k_F\beta\hat{c}[1-\hat{\Gamma}\hat{\kappa}]-\beta k_{F_{\text{ions}}}-\psi_s D_s\hat{\Gamma}\frac{\partial^2\hat{\kappa}}{\partial\hat{s}^2}, \tag{4}$$

where β is the molar volume, $\hat{s}$ is the arc length along the coating front, and ψ_s is the thickness of the coating film that participates in the surface diffusion phenomenon. The units for β are determined by $\beta=(\text{mwt})(1/\text{density})=\text{vol/mole}$, where the density is that for the coating in the solid phase and mwt is the molecular weight of the coating material.

All of the terms in Eq. (4) are evaluated on the front, $\hat{r}=\hat{F}(\theta,\hat{t})$. The first two terms in this equation are the contributions to the normal velocity due to deposition and desorption, and the third term is diffusion along the coating surface. Here D_s is the diffusivity of the adatoms on the coating surface.

The coating surface is given by

$$\vec{\hat{r}}(\theta,\hat{t})=\hat{F}(\theta,\hat{t})[\cos\theta\vec{i}+\sin\theta\vec{j}], \tag{5}$$

so that the curvature of the front is

$$\hat{\kappa}(\theta,\hat{t})=\frac{\hat{F}^2(\theta,\hat{t})+2\hat{F}_\theta^2(\theta,\hat{t})-\hat{F}(\theta,\hat{t})\hat{F}_{\theta\theta}(\theta,\hat{t})}{[\hat{F}_\theta^2(\theta,\hat{t})+\hat{F}^2(\theta,\hat{t})]^{3/2}}. \tag{6}$$

The normal vector to the coating front is

$$\hat{n}=\frac{\langle\hat{F}_\theta\sin\theta+\hat{F}\cos\theta,-\hat{F}_\theta\cos\theta+\hat{F}\sin\theta\rangle}{\sqrt{\hat{F}_\theta^2+\hat{F}^2}}. \tag{7}$$

The normal front velocity, $\hat{v}_n$, is also defined by

$$\hat{v}_n=\frac{d\vec{\hat{r}}}{d\hat{t}}\cdot\hat{n}. \tag{8}$$

Setting Eq. (4) equal to Eq. (8) allows one to develop an evolution equation for the shape of the coating front.

The governing equations and boundary conditions are nondimensionalized using the following scalings:

Dimensional variable	Scale
$\hat{c}$	C^*
$\hat{r}$	$\hat{S}_F$
$\hat{t}$	$\hat{S}_F/(K_F\beta C^*)$
$\hat{s}$-arc length	$\hat{S}_F$

where K_F is a constant representing the average value of k_F. Dimensionless variables are hatless. These scalings lead to the following nondimensional groups:

$$D_{k_F} = (k_F \hat{S}_F)/\hat{D},$$

$$\Gamma = \hat{\Gamma}/\hat{S}_F,$$

$$Q_F = \frac{K_F \hat{S}_F \beta C^*}{\hat{D}} \ll 1,$$

where D_{k_F}, the Damköhler number, is the ratio of the rate of deposition on the fiber to the rate of neutral species transport by diffusion, and Q_F is the ratio of the rate of front motion to the rate of diffusion of the neutral species.

The nondimensional governing equation for concentration is

$$Q_F c_t = c_{rr} + \frac{1}{r}c_r + \frac{1}{r^2}c_{\theta\theta}, \quad \text{for} \quad F(\theta,t) < r < 1. \tag{9}$$

Here, $F(\theta,t)=\hat{F}(\theta,\hat{t})/\hat{S}_F$ is the dimensionless coating thickness. We impose two spatial boundary conditions upon the concentration field. At the edge of the local region ($r=1$), the concentration is uniform as predicted by the reactor-scale model

$$c = 1. \tag{10}$$

At the edge of the coating ($r=F(\theta,t)$), we apply the dimensionless version of Eq. (3),

$$\frac{c_r - (F_\theta/F^2)c_\theta}{\sqrt{1+(F_\theta/F)^2}} = D_{k_F} c[1-\Gamma\kappa] - \frac{k_{F_{\text{ions}}}\hat{S}_F}{C^*\hat{D}}, \tag{11}$$

where

$$\kappa = \frac{F^2 + 2F_\theta^2 - FF_{\theta\theta}}{[F^2+F_\theta^2]^{3/2}} \tag{12}$$

is the nondimensional curvature.

The coating front velocity (4) in dimensionless form is

$$\frac{\langle F_t \cos\theta, F_t \sin\theta\rangle \cdot \langle (F\sin\theta)_\theta, (-F\cos\theta)_\theta\rangle}{\sqrt{F_\theta^2+F^2}} = \frac{k_F}{K_F}c[1-\Gamma\kappa] - \frac{k_{F_{\text{ions}}}}{K_F C^*} - \frac{\psi_s D_s}{\beta C^* K_F \hat{S}_F^2}\Gamma\frac{\partial^2\kappa}{\partial s^2}. \tag{13}$$

Note that $\partial^2\kappa/\partial s^2 = (\kappa_\theta/\sqrt{F^2+F_\theta^2})_\theta/\sqrt{F^2+F_\theta^2}$ is the second derivative of the curvature with respect to arc length, and so Eq. (13) takes the form

$$\frac{FF_t}{\sqrt{F^2+F_\theta^2}} = \frac{k_F}{K_F}c[1-\Gamma\kappa] - \frac{k_{F_{\text{ions}}}}{K_F C^*} - \frac{\psi_s D_s \Gamma}{\beta C^* K_F \hat{S}_F^2}\frac{(\kappa_\theta/\sqrt{F^2+F_\theta^2})_\theta}{\sqrt{F^2+F_\theta^2}}. \tag{14}$$

A similar axisymmetric version of this evolution equation has been derived and solved in Ref. 10.

References 9 and 10 solve Eqs. (9)–(14) by assuming that c is independent of θ, and by evaluating Eq. (11) at r_F, the average initial radius of the uncoated nanofiber. Under these approximations, the concentration field is not affected by perturbations in the coating surface. These approximations are not made in the present numerical simulations.

B. Numerical simulations

In the level set formulation, the position of the deposition front is tracked implicitly by the signed distance function $\phi=\phi(\vec{x},t)$ (where $\phi=0$ corresponds to the location, $F(\theta,t)$, of the front at time t). One method of tracking the evolution of such interfaces is that introduced by Ref. 14. The evolution of the signed distance function is determined by

$$\frac{\partial\phi}{\partial t} + V|\nabla\phi| = 0, \tag{15}$$

where V is the extension velocity field. This velocity is a function defined everywhere such that it matches $\hat{v}_n$ given above for the normal front velocity at locations where $\phi=0$. In the results presented in this work, the above equation was approximated using a conservative scheme[15] for nonlinear Hamilton–Jacobi equations with convex Hamiltonian utilizing fourth order Weighted Essentially Non-Oscillatory (WENO) approximations of the spatial derivatives and a third order Total Variation Diminishing (TVD) Runge–Kutta approximation for the time derivative. Fourth order differencing of the curvature and surface Laplacian terms in Eq. (13) was accomplished utilizing the formulation proposed by Ref. 16. In this work, we also utilize a localized ("tube") level set method as described in Ref. 17, so that the level set equations are only solved in a localized band of grid cells centered around the zero level set.

Growth of the fiber coating is slow compared to the diffusion of the materials to the deposition front. As a result, at each time step of the front evolution [controlled by Eq. (15)], one must solve the steady-state version of Eq. (9): with the boundary conditions (10) and (11). Because this work utilizes a very refined grid near the deposition front, this steady-state diffusion equation was solved on a nonuniform grid with the smallest cells (near the front) being 1/2400th of the computational domain, and the largest (near the outer boundary) being 1/150th. For details concerning such approaches see (for example).[18]

The full concentration problem (9) is solved for the standard parameter set in Table I and varying values of k_F to consider a range of values for D_{k_F}. The concentration at the front is used in the deposition term in the normal velocity expression (13), and hence is needed in the level set algo-

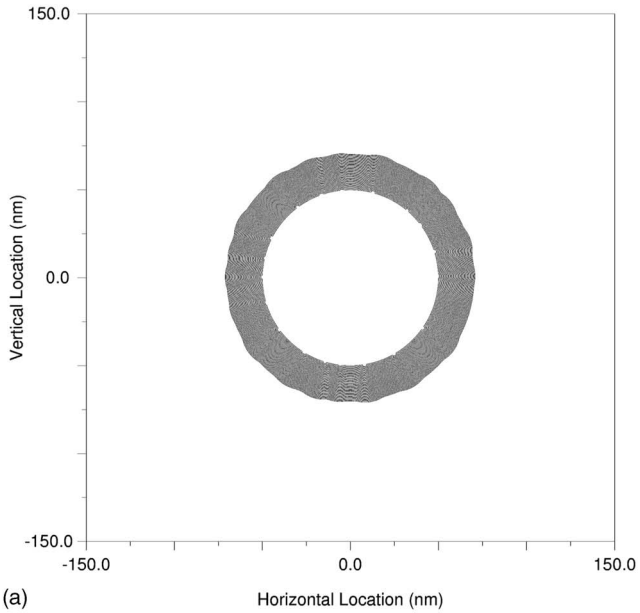

FIG. 2. Morphology of the coating front (contours represent 10 s intervals of growth) for varying values of D_{k_F} and multiple initial bumps. (a) $D_{k_F}=5$, polar geometry. (b) $D_{k_F}=5$, axisymmetric geometry.

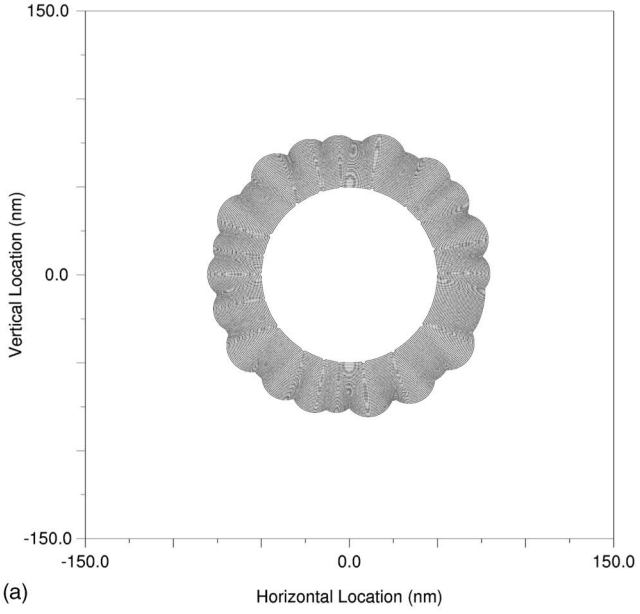

FIG. 3. Morphology of the coating front (contours represent 10 s intervals of growth) for varying values of D_{k_F} and multiple initial bumps. (a) $D_{k_F}=30$, polar geometry. (b) $D_{k_F}=30$, axisymmetric geometry.

rithm to determine $F(\theta,t)$. Ref. 11 conducted benchmarking studies of the model against experimental data using a very similar parameter set, and demonstrated that the model we have developed predicts trends for the coating evolution on nanoscale structures that agree with experimental observation.

III. NUMERICAL SIMULATION RESULTS

References 9–11 focused on the influence of model parameters on the coating thickness, morphology, and wavelength. Basic results indicate that when D_{k_F} is large, the deposition dominates and bumps will grow, leading to a rough surface. When D_{k_F} is small, diffusion dominates and dips will fill in faster, leading to a smoother surface. We continue evaluation of the model predictions by simulating the general trends of coating thickness and morphology in response to parameter changes.

Figures 2–6 depict the morphology of the coating, in polar and axisymmetric geometries, as the Damköhler number increases. The contours shown in these figures represent the coating front locations at 10 s intervals of growth. Specifically, we varied the value of k_F from 10^{13} to 10^{15} mole/nm^2 s, while holding $\hat{S}_F$ and $\hat{D}$ fixed, to vary D_{k_F} in these figures. Additionally, for these simulations the initial fiber radius is 50 nm. The parameter set, Table I, leads to a coating thickness of around 30 nm in 6 min of deposition time, consistent with experimental observation.[11] The initial fiber shape is circular with 0.5–1 nm high by 1–3 nm wide bumps superposed on the fiber surface at random locations

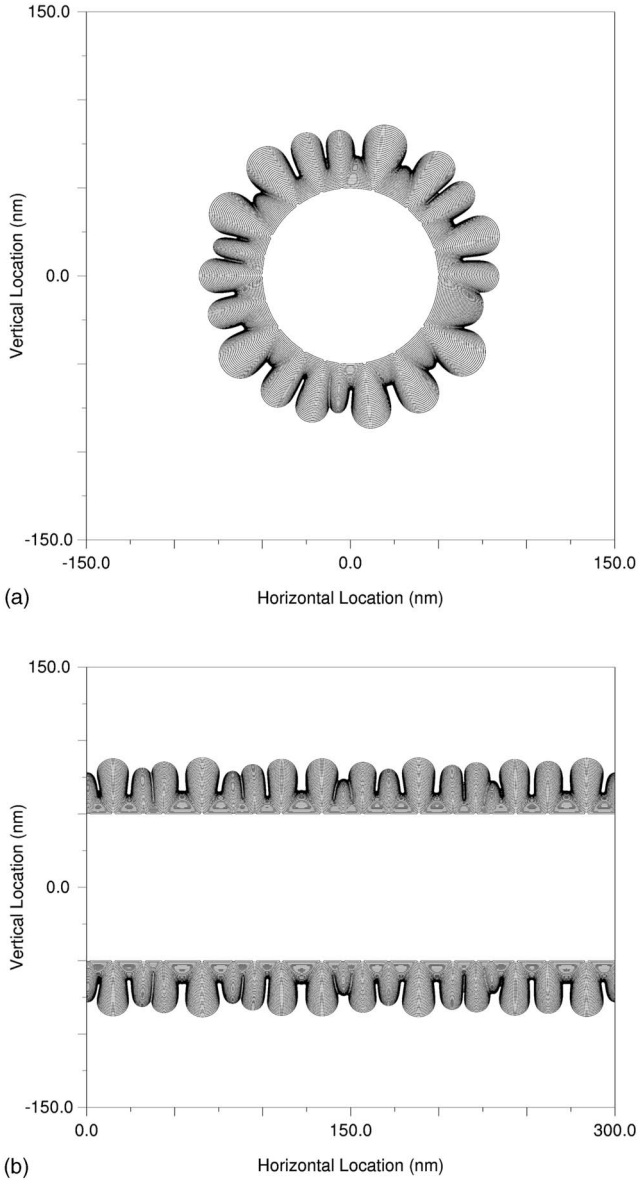

FIG. 4. Morphology of the coating front (contours represent 10 s intervals of growth) for varying values of D_{k_F} and multiple initial bumps. (a) $D_{k_F}=75$, polar geometry. (b) $D_{k_F}=75$, axisymmetric geometry.

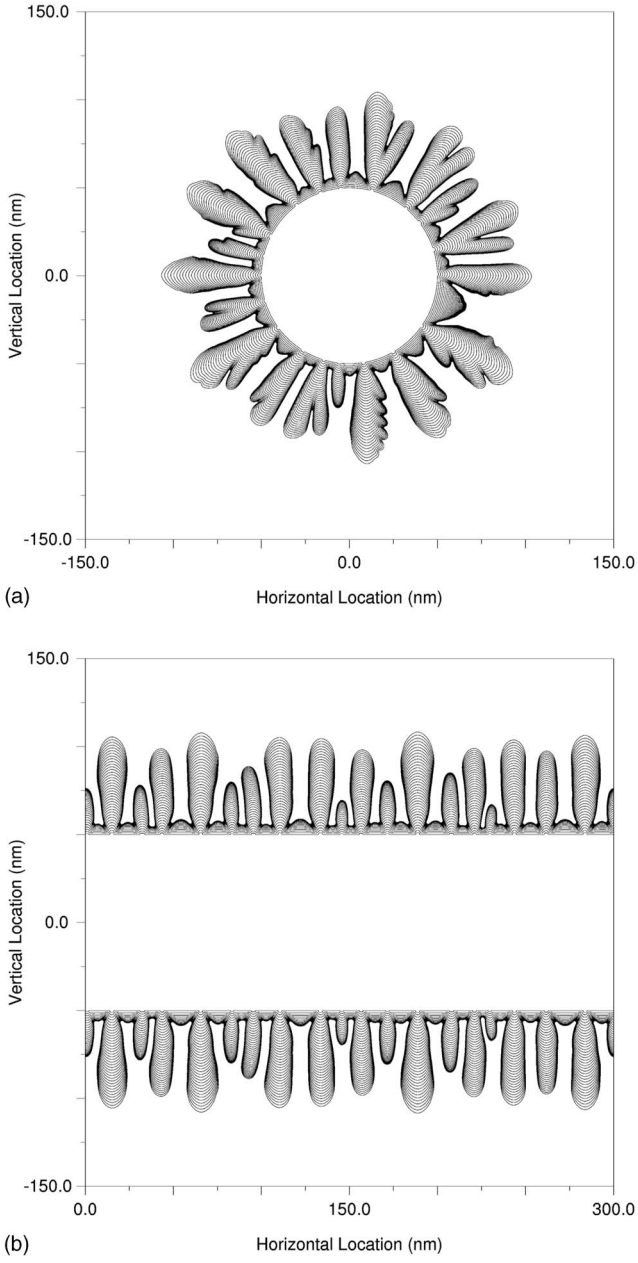

FIG. 5. Morphology of the coating front (contours represent 10 s intervals of growth) for varying values of D_{k_F} and multiple initial bumps. (a) $D_{k_F}=300$, polar geometry. (b) $D_{k_F}=300$, axisymmetric geometry.

around the circular surface. At small values of D_{k_F} the simulations predict a wavy type coating. As D_{k_F} increases the coating morphology becomes nodular. Further increases in D_{k_F} result in dendritic looking needles.

As the coating first develops a mushroom-type shape for the nodular morphology, the pinching together of the peaks may result in a further reduction of concentration in the valleys. This causes the peaks to grow faster than the valleys and a needlelike formation results. This phenomenon, known as self-shadowing, has also been considered by[19] through the inclusion of relevant view factors for the impinging concentration flux over the surface, and by[20–22] for coating onto flat surfaces.

These results are summarized in practical terms as follows. Reference 9 finds that in a PEPVD reactor, k_F increases with power and pressure, both of which increase the kinetic energies of the adatoms, and decreasing angle of incidence of the adatoms toward the surface (measured from the normal to the surface). Hence, smooth coatings may be achieved with lower power and pressure, while rough coatings may result from higher power and pressure. This statement is valid given that the angle of alignment of the fibers relative to the sputtering target is constant.

Figure 7 displays the calculated morphology of the coating for $D_{k_F}=600$ and a single initial bump located at the $\theta=0$ location on the fiber surface. The perturbation obviously leads to the growth of more than just the one needle, and the growth is remarkably symmetric. This indicates that under these growth conditions, a single small defect in the fiber shape, or perhaps a small particle from homogeneous nucleation in the PEPVD chamber, could lead to a drastic change in the coating morphology from a uniform circular shape.

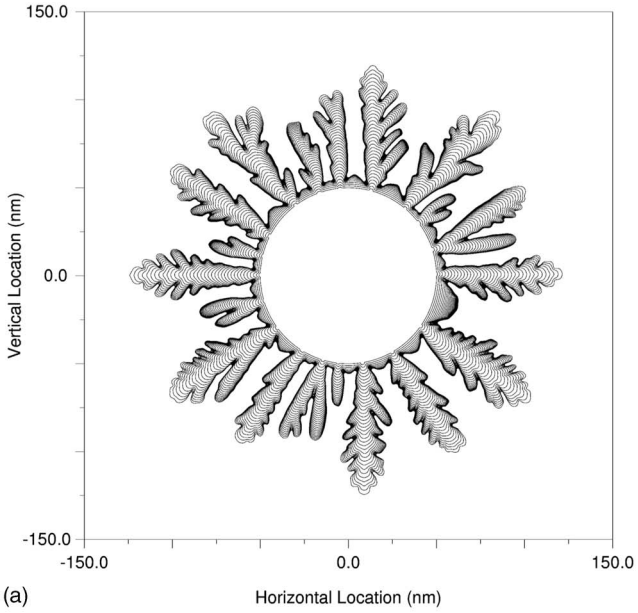

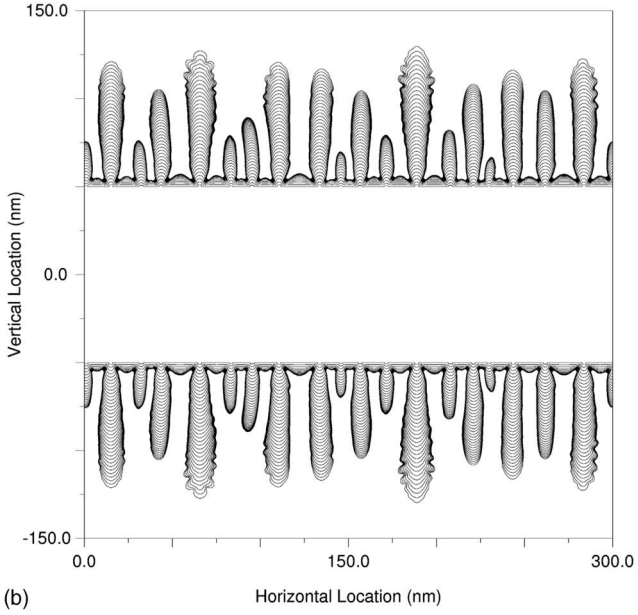

FIG. 6. Morphology of the coating front (contours represent 10 s intervals of growth) for varying values of D_{k_F} and multiple initial bumps. (a) $D_{k_F}=600$, polar geometry. (b) $D_{k_F}=600$, axisymmetric geometry.

IV. SUMMARY AND CONCLUSION

The coating of nanoscale structures and the evolution of crystalline structure at the nanoscale are and will continue to be important issues. We have developed a comprehensive model integrating across atomic to continuum length scales for simulating the sputtering, transport, and deposition of coating material onto a nanoscale substrate.[8–11] In this paper we conduct numerical simulations of the concentration field that couple with level set simulations of the evolution equation for the coating free surface. The model simulations predict that as the Damköhler number is increased the coating morphology changes from a wavy to a nodular to a needle-type form as observed experimentally and shown in Figs. 1(a)–1(c).

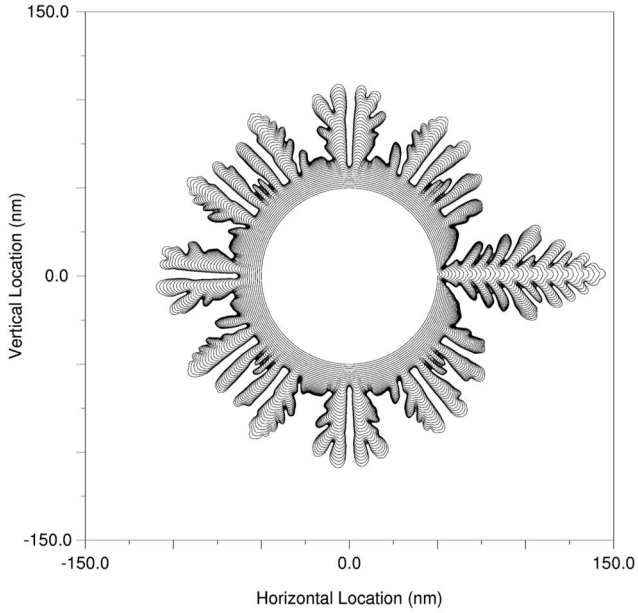

FIG. 7. Morphology of the coating front (contours represent 10 s intervals of growth) for $D_{k_F}=600$ and a single initial bump located at $\theta=0$.

Based upon this study and the parametric study of material parameters in Refs. 8–11 it appears that systems characterized by small attachment rates k_F, high diffusive transport of material, high surface diffusion, and high etching of coating material will have smoother coatings. On the other hand, systems characterized by high attachment rates k_F will have rougher coatings that may eventually become nodular or needlelike in shape. These results are easily summarized through inspection of Eq. (4). As the first term of this normal front velocity expression, the deposition term, becomes larger than the etching and surface diffusion terms, the morphology of the coating changes from smooth to rough.

With a validated model we can begin to predict how coating properties will change with deposition conditions for similar geometries. This predictive capability will be quite useful as the size of solid state optoelectronic components continues to decrease.

ACKNOWLEDGMENTS

This work was supported by the NSF under Grant No. DMI-0403835 and by NASA under Grant No. NNC-04GB27G.

[1]E. T. Bender, R. Wang, M. T. Aljarrah, E. A. Evans, and R. D. Ramsier, J. Vac. Sci. Technol. **25**, 922 (2007).
[2]B. Y. Deng, Q. F. Wei, and W. D. Gao, J. Coat. Technol. Res. **5**, 393 (2008).
[3]D. H. Reneker, A. L. Yarin, E. Zussman, and H. Xu, Adv. Appl. Mech. **41**, 43 (2007).
[4]Y. Ito, H. Hasuda, M. Kamiktakahara, C. Ohtsuki, M. Tanihara, I. K. Kang, and O. H. Kwon, J. Biosci. Bioeng. **100**, 43 (2005).
[5]Y. Gao, P. He, J. Lian, L. M. Wang, D. Qian, J. Zhao, W. Wang, M. J. Schulz, J. Zhang, X. P. Zhou, and D. L. Shi, J. Macromol. Sci., Phys. **45**, 671 (2006).
[6]Q. F. Wei, H. Ye, D. Y. Hou, W. B. Wang, and W. D. Gao, J. Appl. Polym. Sci. **99**, 2384 (2006).
[7]Y. B. Cai, F. L. Huang, Q. F. Wei, E. Wu, and W. D. Gao, Appl. Surf. Sci. **254**, 5501 (2008).
[8]A. Buldum, I. Busuladzic, C. B. Clemons, L. H. Dill, K. L. Kreider, G. W.

Young, E. A. Evans, G. Zhang, S. I. Hariharan, and W. Keifer, J. Appl. Phys. **98**, 044303 (2005a).
[9]A. Buldum, C. B. Clemons, L. H. Dill, J. Heminger, K. L. Kreider, G. W. Young, X. Zheng, E. A. Evans, G. Zhang, and S. I. Hariharan, J. Appl. Phys. **98**, 044304 (2005b).
[10]K. Moore, C. Clemons, K. L. Kreider, and G. Young, J. Appl. Phys. **101**, 064305 (2007).
[11]C. B. Clemons, P. Hamrick, J. Heminger, K. Kreider, G. W. Young, A. Zheng, E. A. Evans, and G. Zhang, J. Appl. Phys. **103**, 044304 (2008b).
[12]W. Liu, M. Graham, E. A. Evans, and D. H. Reneker, J. Mater. Res. **17**, 3206 (2002).
[13]M. A. Lieberman and A. J. Lichtenberg, *Principles of Plasma Discharges and Materials Processing* (Wiley, New York, 1994).
[14]S. Osher and J. A. Sethian, J. Comput. Phys. **79**, 12 (1988b).
[15]J. A. Sethian, *Level Set Methods and Fast Marching Methods* (Cambridge University Press, Cambridge, England, 1999).
[16]D. L. Chopp and J. A. Sethian, Interfaces Free Boundaries **1**, 1 (1999).
[17]D. Peng, B. Merriman, S. Osher, H. Zhao, and M. Kang, J. Comput. Phys. **155**, 410 (1999b).
[18]J. W. Thomas, *Numerical Partial Differential Equations: Conservation Laws and Elliptic Equations* (Springer, New York, 1995).
[19]O. A. Louchev, Y. Sato, and H. Kanda, J. Appl. Phys. **89**, 2151 (2001).
[20]J. Thiart and V. Hlavacek, J. Comput. Phys. **125**, 262 (1996).
[21]J. Thiart and V. Hlavacek, AIChE J. **41**, 1926 (1995).
[22]G. S. Bales, A. C. Redfield, and A. Zangwill, Phys. Rev. Lett. **62**, 776 (1989).